Imaging transient melting of a nanocrystal using an X-ray laser

Jesse N. Clark[a,b,c,1], Loren Beitra[a], Gang Xiong[a], David M. Fritz[d], Henrik T. Lemke[d], Diling Zhu[d], Matthieu Chollet[d], Garth J. Williams[d], Marc M. Messerschmidt[d], Brian Abbey[e], Ross J. Harder[f], Alexander M. Korsunsky[g,h], Justin S. Wark[i], David A. Reis[b], and Ian K. Robinson[a,h]

[a]London Centre for Nanotechnology, University College London, London WC1E 6BT, United Kingdom; [b]Stanford PULSE Institute, SLAC National Accelerator Laboratory, Menlo Park, CA 94025; [c]Center for Free-Electron Laser Science, Deutsches Elektronensynchrotron, 22607 Hamburg, Germany; [d]Linac Coherent Light Source, SLAC National Accelerator Laboratory, Menlo Park, CA 94025; [e]Australian Research Council Centre of Excellence for Advanced Molecular Imaging, La Trobe University, Bundoora, VIC 3086, Australia; [f]Advanced Photon Source, Argonne National Laboratory, Argonne, IL 60439; [g]Department of Engineering Science, University of Oxford, Oxford OX1 3PJ, United Kingdom; [h]Research Complex at Harwell, Didcot, Oxfordshire OX11 0DE, United Kingdom; and [i]Department of Physics, Clarendon Laboratory, University of Oxford, Oxford OX1 3PU, United Kingdom

Edited by Henry C. Kapteyn, University of Colorado Boulder, Boulder, CO, and approved May 5, 2015 (received for review September 12, 2014)

There is a fundamental interest in studying photoinduced dynamics in nanoparticles and nanostructures as it provides insight into their mechanical and thermal properties out of equilibrium and during phase transitions. Nanoparticles can display significantly different properties from the bulk, which is due to the interplay between their size, morphology, crystallinity, defect concentration, and surface properties. Particularly interesting scenarios arise when nanoparticles undergo phase transitions, such as melting induced by an optical laser. Current theoretical evidence suggests that nanoparticles can undergo reversible nonhomogenous melting with the formation of a core-shell structure consisting of a liquid outer layer. To date, studies from ensembles of nanoparticles have tentatively suggested that such mechanisms are present. Here we demonstrate imaging transient melting and softening of the acoustic phonon modes of an individual gold nanocrystal, using an X-ray free electron laser. The results demonstrate that the transient melting is reversible and nonhomogenous, consistent with a core-shell model of melting. The results have implications for understanding transient processes in nanoparticles and determining their elastic properties as they undergo phase transitions.

X-ray laser | coherent diffraction | phase transition | ultrafast imaging | pump-probe

Nanoparticles also display interesting properties due to their size and morphology; for example, they can exhibit anomalously low thermal conductivity due to the phonon mean free path approaching the size of the particle. This has significant implications for developing novel thermoelectric devices (1). Further interest in transient processes in nanoparticles comes from their role in photoacoustic imaging (2) and photothermal cancer therapy (3) and their potential in high-harmonic generation (4). Therefore, it is critical from both a fundamental and a practical point of view to understand the photon, electron, and lattice interactions of nanoparticles irradiated with a short pulse (<100 fs) laser up to the point of melting.

Molecular dynamics (MD) simulations have provided the most detailed models of the nanoparticles' response to laser irradiation at low intensity, with reversible nonhomogenous surface premelting predicted (5, 6). The simulations indicated that isolated regions on the nanoparticle surface begin to melt before forming a continuous layer. Additionally, these simulations suggest that before the formation of a nonhomogenous liquid outer layer surrounding a solid inner core, preferential facet premelting can occur with liquid-like atoms appearing first in the (100) and (110) crystallographic directions. It was also observed that during the formation of the liquid outer layer, liquid regions extended inward toward the solid core. Simulations on larger nanorods (7) have suggested more exotic behavior during laser-induced premelting, such as internal structural changes from face-centered cubic to hexagonal close-packed structures along with the formation of surface defects. Dislocation cores were found to nucleate on the crystal surface with stacking faults forming and propagating toward the interior. An important result found in the simulations was surface premelting arising before the formation of defects. This suggests that surface premelting can initiate without the formation of defects acting as surface nucleation sites.

Previous experimental (8–11) investigations of nanoparticles using pump-probe experiments have alluded to partial melting of the nanoparticles occurring at much lower temperatures than that of the bulk (9). It has been proposed that the formation of a liquid outer shell occurs at temperatures as low as 70% of the melting temperature and within 100 ps of irradiation (9). However, this is yet to be observed directly. It has also been suggested that raising the temperature of nanoparticles to 100 °C can facilitate surface premelting (10). The formation of a liquid outer shell is something that has been observed in static experiments (12) but has yet to be confirmed on a picosecond timescale. It is speculated that for temperatures below the melting temperature, the process of liquid-shell formation is reversible (5, 9, 12). However, this is still largely unconfirmed and the degree of reversibility is still an open question. The main distinction between a solid and a liquid metal is not its density, but the presence (or absence) of long-range order. Consequently, resolving the mechanisms of

Significance

Despite phase transitions, such as melting, being ubiquitous in nature, understanding what occurs at the nanoscale (such as in nanocrystals) has so far remained challenging. With ensemble studies of nanocrystals it is often difficult to discriminate between intrinsic size-dependent properties and effects due to sample size and shape dispersity. Here, using an X-ray free electron laser we image the reversible melting of an individual nanocrystal induced by an ultrashort laser. It is revealed that the melting occurs transiently, repeatably, and inhomogeneously. This is consistent with a core-shell model where the exterior is melted and a solid core remains. These findings reveal, unambiguously, that core-shell melting occurs, which has important implications for understanding nanoscale phenomena.

Author contributions: J.N.C., L.B., G.J.W., R.J.H., and I.K.R. designed research; J.N.C., L.B., G.X., D.M.F., H.T.L., D.Z., M.C., G.J.W., M.M.M., B.A., R.J.H., A.M.K., J.S.W., D.A.R., and I.K.R. performed research; J.N.C. and I.K.R. analyzed data; and J.N.C., D.A.R., and I.K.R. wrote the paper.

The authors declare no conflict of interest.

This article is a PNAS Direct Submission.

[1]To whom correspondence should be addressed. Email: jn2clark@slac.stanford.edu.

This article contains supporting information online at www.pnas.org/lookup/suppl/doi:10.1073/pnas.1417678112/-/DCSupplemental.

partial melting in individual nanoparticles requires imaging with diffracting probes such as X-rays or electrons.

Results and Discussion

Experiment. To investigate transient melting in nanocrystals, an experiment was carried out using the X-ray Pump Probe instrument at the Linac Coherent Light Source (LCLS) (13), an X-ray fee electron laser (XFEL) at the SLAC National Laboratory with a schematic shown in Fig. S1. One hundred-femtosecond [full width, half duration (FWHD)], 9.2-KeV X-ray pulses (120 Hz) were monochromatized by a silicon monochromator before being focused by beryllium refractive lenses (*Materials and Methods, Experiment*). The sample consisted of gold nanocrystals (*Materials and Methods*) on a silicon nitride membrane mounted vertically and normal to both the optical pump and X-ray probe pulses. Coherent diffraction patterns were recorded using a Cornell-SLAC pixel array detector (CS-PAD) (14) placed 1.2 m from the sample at the gold (111) Bragg peak. Orientation differences between illuminated nanocrystals result in their Bragg peaks being spatially separated on the detector. Transient melting was induced by pumping the sample with a Gaussian [60 × 60-μm full width at half maximum (FWHM)] 800-nm, 50-fs (FWHD) laser, using incident pulse energies of 1–2 μJ. The delay between the pump and probe pulse was varied to provide the time-resolved data. Recording the coherent diffraction on a pixel detector at least twice, the Nyquist frequency allows the diffraction fringes to be resolved and permits direct access to real-space information from the nanocrystal through its autocorrelation (obtained by inverse Fourier transform of the pattern) or the crystal's electron density [by using iterative phase retrieval (15, 16)] as a function of delay time. Additionally, the Fourier transform (with respect to time) can be taken of the intensity. This provides direct access to the phonon dispersion (17), which can then be used to obtain materials properties such as the elastic constants (18).

Time-Resolved Diffraction Data. Shown in Fig. 1*A* are selected 2D data collected from the same individual nanocrystal as a function of delay time (horizontally) and pulse energy (vertically), showing the scattering vectors parallel ($q_{\|}$) and perpendicular ($q_{\perp}$) to the gold (111) Bragg peak. At the lowest energy (1 μJ), small peak shifts and some broadening are evident as the delay time increases. For small perturbations, the peak shift can be interpreted as homogenous strain (expansion and contraction of the lattice) whereas the distortion can be interpreted as inhomogeneous strain. The diffraction pattern becomes significantly distorted (particularly at +50 ps) for the highest energy (Movie S1) and has shifted considerably while becoming elongated and broad in the direction of the scattering vector. The larger shift can be broadly interpreted as an increase in average lattice temperature (compared with the lower energies) whereas the broadening of the peak may no longer be simply due to inhomogenous strain but also be due to a morphology (size) change of the nanocrystal (19), in which its crystalline volume is transiently reduced, suggesting that the crystal is transiently melted.

The oscillatory component of the data can be seen in Fig. 1*B*, which shows the diffraction parallel to the (111) scattering vector ($q_{\|}$) as a function of delay time for the three energies at three different $q_{\perp}$ scattering values (indicated by the gray lines in Fig. 1*A*). The highest energy displays a periodic loss of intensity (in addition to broadening), something that is consistent with a picture of the nanocrystal undergoing transient melting and recrystallization. For the highest pump energy, the intensity drops to $\approx 40\%$ of the value of the negative delay times and provides an estimate of the change in diffracting volume of the nanocrystal.

If these results were explained using a classical interpretation of simple heating, a linear increase in pulse energy (or fluence) should produce a commensurate linear increase in the lattice spacing (and peak shift) (20). To examine the linearity of the shift in our data, the center of mass of each diffraction peak is plotted in Fig. 2*A* as a function of pulse energy. This plot illustrates the classical thermal expansion (that an increase in temperature leads to an increase in lattice spacing) and subsequent departure from this at the highest pulse energy. We also note that the temperature dependence on the thermal expansion coefficient should cause larger shifts with increasing pulse energy (anharmonicity), which is in the opposite direction to what is observed. The temperature difference (interpreted classically) during the oscillation obtained from the peak shift is 250 K, which compares to an estimated temperature increase from an XFEL pulse of ≈ 67 K (*SI Materials and Methods*). The nonlinear peak shift as a function of pulse energy is shown in Fig. 2*C*,

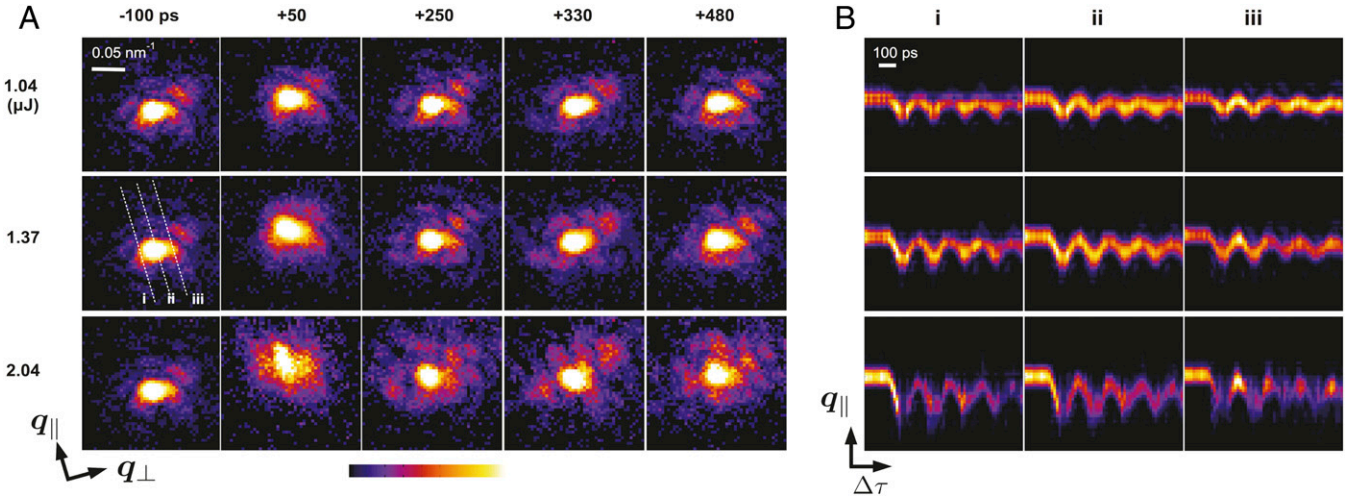

Fig. 1. Diffraction data from a single nanocrystal. (*A*) Diffraction from a single gold nanocrystal as a function of pump-laser pulse energy (vertical) and pump-probe delay time (horizontal). Significant nonlinear broadening of the peak occurs at the highest pulse energy. $\boldsymbol{q}_{\|}$ points in the direction of the off-specular gold (111) scattering vector. (*B*) Slices for different planes (horizontally) parallel to the scattering vector for delay time showing the oscillatory motion of the Bragg peak for the different pulse energies (vertically). The amplitude of the peak shift increases with increasing pump pulse energy with significant distortion and loss of intensity evident at the highest pulse energy. The locations of the three slices can be seen in *A* for −100 ps at 1.37 μJ.

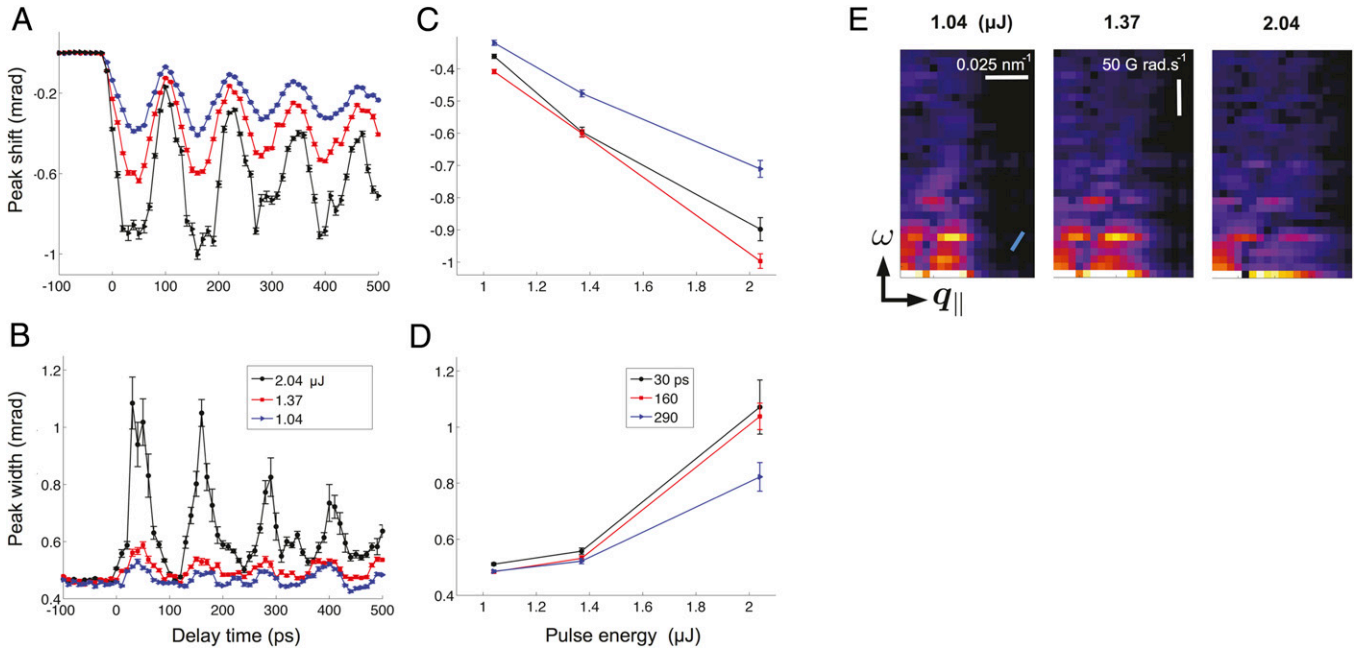

Fig. 2. Time-dependent peak position and width for a single nanocrystal. (*A* and *B*) The center of mass (*A*) and peak width (*B*) (full width at half maximum) as a function of delay time for the three different pulse energies. Nonlinear peak shift and peak broadening can be observed for three different times in *C* and *D*, respectively (the lines are a guide to the eye only). The nonlinear peak shift can be attributed to partial melting of the surface with the subsequent size change resulting in a nonlinear broadening. (*E*) By taking the time Fourier transform of the data, the dispersion of the LA phonons is obtained, showing a softening of the phonon modes for the highest pulse energy. The slope of the dispersion gives the speed of sound in the nanocrystal and is compared with bulk values (the slope of the pale blue line, $\approx$ 3,700 m·s^{-1}).

which plots the peak shift for selected times. The nonlinearity is also evident in the peak width, which is shown in Fig. 2*D* and plotted as a function of pulse energy for select times where the width was taken as the full width at half maximum of the peak projected along $q_{\perp}$. As mentioned earlier, the peak broadening is due in large part to inhomogeneous strain, although changes in particle size or morphology can contribute. As is known from powder diffraction, peak width is linearly proportional to strain and inversely proportional to crystallite size (19). The point that the peak width increases rapidly (+50 ps) also coincides with a plateau in peak shift. This can be explained if the particle is undergoing some transient surface melting. The plateau may be caused by the energy no longer going into heating the lattice but instead as latent heat of fusion to partially melt the particle, so that the temperature saturates at the melting point. The rapid increase in peak width combined with the plateau in peak shift supports the view that either the particle size is reduced or there is a gross change in morphology. The transient nature of the partial melting is evident in the same behavior at larger pump-probe delays.

Further evidence for the occurrence of transient melting can be seen in the significant softening of the longitudinal acoustic phonons, which is shown in Fig. 2*E*. The low-angle, low-frequency component of the dispersion is obtained as a time-Fourier transform (17) of the data (after subtraction of the −100-ps delay time), which for a cubic crystal can give the speed of sound from the gradient of the scattering vector with frequency. The speed of sound for Au along the (111) direction is shown as the gradient of the pale blue line and clearly shows the softening at the highest pulse energy, with a reduction of $\approx$25%. Interestingly, partial quantization is evident in the dispersion curve (in both temporal and spatial directions) due to the finite size of the nanocrystal and the coherence of the X-rays (speckles). We note the importance of being able to obtain such information on individual nanocrystals, particularly related to heat transport in nanosystems (21).

Real-Space Images. Deconvolution of the effects of size and strain in relation to peak broadening is a key question in this study. Conventionally (19, 22), we would need to record diffraction from two or more Bragg peaks to distinguish these effects. We can, however, answer the question in a model-independent way, using coherent diffraction imaging (CDI) (23) to image the crystal at each time delay. CDI is an imaging technique that replaces the physical image forming the optic (i.e., lens) with a pixel detector and an iterative algorithm (i.e., a "virtual lens"), offering the potential for wavelength-limited resolution. Provided a coherent wave field (e.g., X-rays, electrons, or visible light) illuminates an isolated object using a geometry that allows adequate sampling of the diffraction pattern, real-space images can be obtained via iterative phase retrieval (24). Adequate sampling refers to having the number of independently measured points (from the data) being greater than the number of unknowns (25). Examples of CDI include imaging carbon nanotubes (26) at near atomic resolution, the deformation field inside a nanocrystal (15), individual viruses (27), and acoustic phonons (16).

As the data were collected from a single nanocrystal, using coherent X-rays with a geometry to allow adequate sampling of the diffraction pattern, real-space images could be obtained via iterative phase retrieval. A phase retrieval algorithm was developed and used to exploit the redundancy of the time-resolved data (*SI Materials and Methods* and Fig. S2). Shown in Fig. 3 are images of the projected density (Fig. 3*A*) and local lattice displacement (Fig. 3*B*) for the (111) Bragg peak (Movies S2 and S3, respectively) at a resolution of 60 nm [determined from the phase retrieval transfer function (28)]. One feature of this particular nanocrystal is the small stacking-fault structure on the left-hand edge. This absence of density can be interpreted as a twinned region that does not satisfy the Bragg condition. The morphology

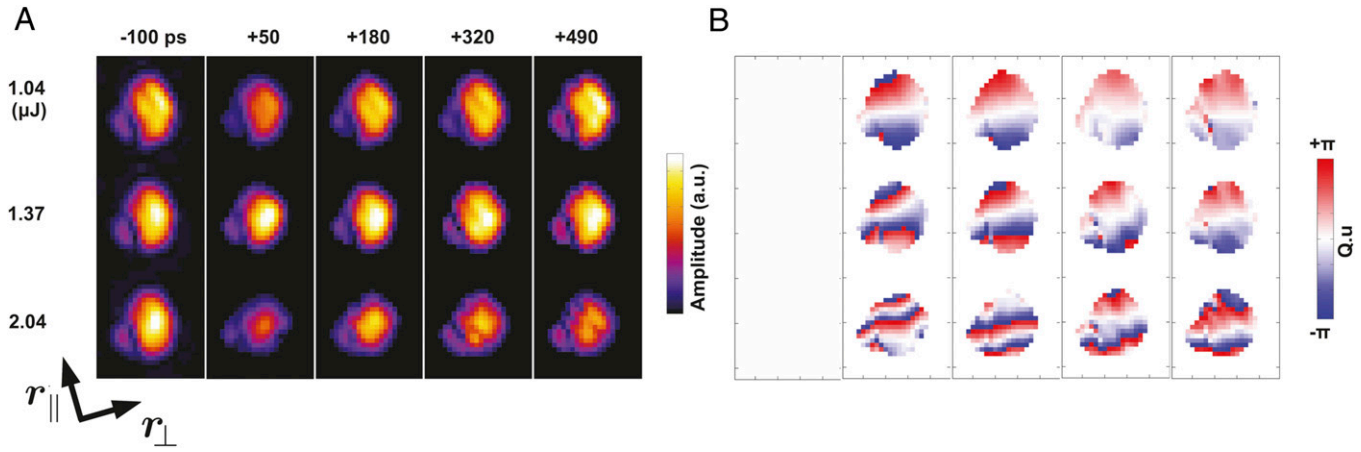

Fig. 3. Real-space images of a nanocrystal undergoing transient melting. (*A*) Recovered real-space images for selected times (horizontally) and as a function of pulse energy (vertically). Significant morphology changes are apparent for the highest pulse energy, consistent with a loss of crystallinity attributed to surface melting. The most dramatic changes occur at the point where the greatest nonlinearity occurs (+50 ps). (*B*) Recovered images of the phase (modulo 2π or 1 lattice spacing) after subtraction of the −100-ps time. The phase shows the projected displacement as a function of time (horizontally) and pulse energy (vertically). (Scale bar, 200 nm.)

of the crystal is well reproduced for the lowest pulse energy for all delay times. As the pulse energy is increased it is evident that the morphology and size of the nanocrystal change dramatically. At the moment of greatest broadening (+50 ps, 2.04 μJ), the crystal has the narrowest core and thickest "halo" of lower density. We interpret this image as a crystalline core surrounded by partially ordered liquid. This change and partial restoration of the shape (with time) is consistent with a partial melting of the outer layer of the nanocrystal. This assertion is also corroborated by the time-dependent autocorrelation (Fig. S3) whose boundary provides information on the size and any change in shape of the nanocrystal (*SI Materials and Methods*) and is obtained directly from the data without phase retrieval.

To eliminate the possibility that the observed density changes are not in fact due to a shift along the third reciprocal space direction, simulations of the expected data and autocorrelation were calculated for the experimental conditions (including noise) and are shown in Fig. S4. This demonstrates that even large shifts (compared with those observed) result in negligible changes. Fig. 3*B* shows that the deformation increases with increasing pulse energy as well as increasing at the delay times that show the largest peak shift and increase in width. A notable feature that is present in the highest pulse energy images is the corrugated appearance at the edges of the nanocrystal in the projected displacement. This could be attributed to a nonuniformity in the surface layer during melting with a quasi-periodic arrangement of liquid-like regions, supporting the hypotheses of nonhomogenous surface melting. The time-dependent density and deformation change is shown in Fig. 4 *A* and *B*, respectively, which is a cut through the center of the nanocrystal along the real-space direction parallel with the scattering vector ($\boldsymbol{r}_{\|}$) and delay time ($\Delta\tau$). For the highest pulse energy there is a clear retreat of the boundary (with delay time) of the nanocrystal with partial restoration of its extent. The time frame for restoration is longer than the measurement time (500 ps after irradiation) and is instead given by the 120-Hz repetition rate of the experiment. This is consistent with other studies investigating ensemble melting (9). The similarity of the negative delay times for all pulse energies demonstrates the reversibility of the process (Fig. S5) as the highest pulse energy data were collected before the other pulse energies. The gradient of the deformation along the $\boldsymbol{r}_{\|}$ direction is shown and provides some information on the strain. The periodic deformation is evident with some asymmetry present and its subsequent departure from harmonicity at the highest pulse energy. The largest strain is $0.3 \pm 0.01\%$, which is significantly below the bulk strain expected before melting (9). The error

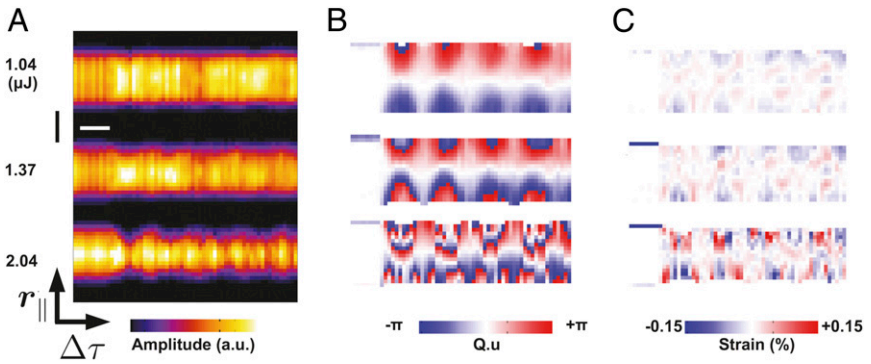

Fig. 4. Time-dependent density, displacement, and strain. (*A*) The time-dependent density shown as a central slice through the nanocrystal for the three plus energies parallel to the direction of the (111) scattering direction. It is evident at the highest pulse energy that there is a morphology and size change. (*B*) The recovered phase shows the deformation through a projection of the displacement field (after subtraction of the initial phase). The magnitude of the deformation grows with the pulse energy. (*C*) The "strain" in the (111) direction is shown, taken from the derivative along the (111) direction. The largest excursions of the Bragg peak coincide with the largest values of the strain. (White scale bar, 100 ps; black scale bar, 200 nm.)

estimate is based on the average SD within the center of the crystal for negative time delays.

Conclusion

In summary, we have been able to observe transient melting in an individual nanocrystal, using an XFEL in a "pump-probe" experiment. We have presented time-resolved images of the retreat of the molten layer following excitation. The results show, primarily, that partial melting occurs in a nonhomogenous fashion with complete restoration of the morphology on every repetition. We have also shown that it is possible to obtain low-frequency and low-wave-vector acoustic phonons from an individual nanocrystal and observed their subsequent softening as transient melting occurs. The results and techniques demonstrated here provide significant insight into phase transitions and dynamics in nanoparticles and will find application in many other areas.

Materials and Methods

Sample Preparation. A 2-nm layer of titanium was deposited using thermal evaporation onto an silicon wafer followed by 20 nm of gold. The thin film was then annealed in air at 1,000 °C for ~10 h after which time the film had dewetted and formed nanocrystals around 300 nm in diameter.

Experiment. The experiment was performed at the XPP instrument at the LCLS. A 1,520 × 1,520-pixel CS-PAD with 110-μm square pixels was used to record the diffraction. Beryllium lenses were positioned to partially focus the X-rays. This regime was chosen so that the X-ray pulses from the LCLS did not destroy the sample. Damage thresholds from either the optical or the X-ray pulses were monitored using a confocal microscope (Olympus LEXT) mounted directly above the sample when the sample was mounted horizontally (rather than vertically when the measurements were made). To record the diffraction patterns, the nanocrystals were aligned to the center of their Bragg peaks. One thousand diffraction patterns were then recorded. Filtering of the data was done ex post facto to remove saturated frames and blank shots (caused by fluctuations in the lasing of the XFEL), with the final summed patterns consisting of the 100 brightest, nonsaturated shots (*SI Materials and Methods*). These data were subsequently inverted using a phase retrieval algorithm (*SI Materials and Methods*) to obtain real-space images of electron density and projected displacement.

ACKNOWLEDGMENTS. This work was supported by an FP7 "Advanced" grant from the European Research Council. I.K.R. is appreciative of support from the Engineering and Physical Sciences Research Council (EPSRC) under Grant EP/I022562/1. J.N.C. gratefully acknowledges financial support from the Volkswagen Foundation. J.S.W. is grateful for support from the UK EPSRC under Grant EP/H035877/1. Portions of this research were carried out at the Linac Coherent Light Source (LCLS) at the SLAC National Accelerator Laboratory. LCLS is an Office of Science User Facility operated for the US Department of Energy Office of Science by Stanford University. Use of the LCLS, SLAC National Accelerator Laboratory, is supported by the US Department of Energy, Office of Science, Office of Basic Energy Sciences under Contract DE-AC02-76SF00515.

1. Kim W, et al. (2006) Thermal conductivity reduction and thermoelectric figure of merit increase by embedding nanoparticles in crystalline semiconductors. *Phys Rev Lett* 96(4):045901.
2. Wang X, et al. (2003) Noninvasive laser-induced photoacoustic tomography for structural and functional in vivo imaging of the brain. *Nat Biotechnol* 21(7):803–806.
3. Gobin AM, et al. (2007) Near-infrared resonant nanoshells for combined optical imaging and photothermal cancer therapy. *Nano Lett* 7(7):1929–1934.
4. Yang Y-Y, et al. (2013) High-harmonic and single attosecond pulse generation using plasmonic field enhancement in ordered arrays of gold nanoparticles with chirped laser pulses. *Opt Express* 21(2):2195–2205.
5. Wang N, Rokhlin SI, Farson DF (2008) Nonhomogeneous surface premelting of Au nanoparticles. *Nanotechnology* 19(41):415701.
6. Wang N, Rokhlin SI, Farson DF (2011) Ultrafast laser melting of Au nanoparticles: Atomistic simulations. *J Nanopart Res* 13:4491–4509.
7. Gan Y, Jiang S (2013) Ultrafast laser-induced premelting and structural transformation of gold nanorod. *J Appl Phys* 113:073507.
8. Hartland GV, Hu M, Dame N, Sader JE (2003) Softening of the symmetric breathing mode in gold particles by laser-induced heating. *J Phys Chem* 107:7472–7478.
9. Plech A, Kotaidis V, Grésillon S, Dahmen C, von Plessen G (2004) Laser-induced heating and melting of gold nanoparticles studied by time-resolved x-ray scattering. *Phys Rev B* 70:1–7.
10. Plech A, et al. (2007) A surface phase transition of supported gold nanoparticles. *Nano Lett* 7:1026–1031.
11. Ruan C-Y, Murooka Y, Raman RK, Murdick RA (2007) Dynamics of size-selected gold nanoparticles studied by ultrafast electron nanocrystallography. *Nano Lett* 7(5):1290–1296.
12. Peters KF, Cohen JB, Chung Y-W (1998) Melting of pb nanocrystals. *Phys Rev B* 57:13430–13438.
13. Emma P, et al. (2010) First lasing and operation of an angstrom-wavelength free-electron laser. *Nat Photon* 4:641–647.
14. Hart P, et al. (2012) The CSPAD megapixel x-ray camera at LCLS. *Proc SPIE* 8504:85040C.
15. Pfeifer MA, Williams GJ, Vartanyants IA, Harder R, Robinson IK (2006) Three-dimensional mapping of a deformation field inside a nanocrystal. *Nature* 442(7098):63–66.
16. Clark JN, et al. (2013) Ultrafast three-dimensional imaging of lattice dynamics in individual gold nanocrystals. *Science* 341(6141):56–59.
17. Trigo M, et al. (2013) Fourier-transform inelastic x-ray scattering from time- and momentum-dependent phonon-phonon correlations. *Nat Phys* 9:790–794.
18. Jurgilaitis A, et al. (2014) Time-resolved X-ray diffraction investigation of the modified phonon dispersion in InSb nanowires. *Nano Lett* 14(2):541–546.
19. Williamson G, Hall W (1953) X-ray line broadening from filed aluminium and wolfram. *Acta Metall* 1(1):22–31.
20. Thomsen C, Grahn HT, Maris HJ, Tauc J (1986) Surface generation and detection of phonons by picosecond light pulses. *Phys Rev B Condens Matter* 34(6):4129–4138.
21. Cahill DG, et al. (2014) Nanoscale thermal transport. II. 2003–2012. *Appl Phys Rev* 1:011305.
22. Warren BE, Averbach BL (1950) The effect of cold-work distortion on x-ray patterns. *J Appl Phys* 21:595–599.
23. Miao J, Charalambous P, Kirz J, Sayre D (1999) Extending the methodology of x-ray crystallography to allow imaging of micrometre-sized non-crystalline specimens. *Nature* 400:342–344.
24. Fienup JR (1982) Phase retrieval algorithms: A comparison. *Appl Opt* 21(15):2758–2769.
25. Miao J, Sayre D, Chapman HN (1998) Phase retrieval from the magnitude of the fourier transforms of nonperiodic objects. *J Opt Soc Am A Opt Image Sci Vis* 15(6):1662–1669.
26. Zuo JM, Vartanyants I, Gao M, Zhang R, Nagahara LA (2003) Atomic resolution imaging of a carbon nanotube from diffraction intensities. *Science* 300(5624):1419–1421.
27. Seibert MM, et al. (2011) Single mimivirus particles intercepted and imaged with an X-ray laser. *Nature* 470(7332):78–81.
28. Chapman HN, et al. (2006) High-resolution ab initio three-dimensional x-ray diffraction microscopy. *J Opt Soc Am A Opt Image Sci Vis* 23(5):1179–1200.